Structure

Article

Structural insights into functional regulation of the human CPEB3 prion by an amyloid-forming segment

Graphical abstract

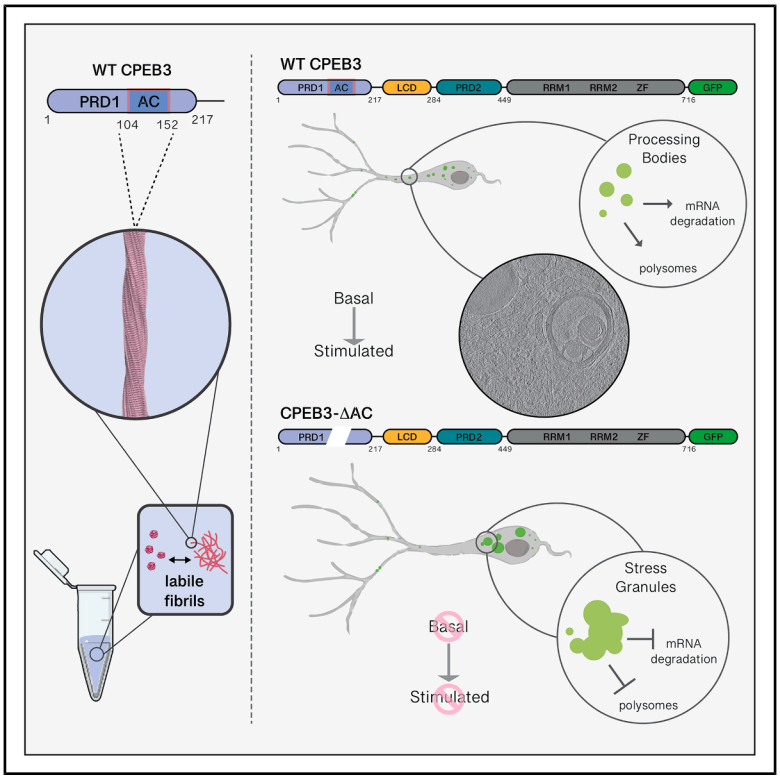

Highlights

- Human CPEB3$_{1\text{-}217}$ self-assembles into labile amyloid fibrils *in vitro*
- The cryo-EM structure of hCPEB3$_{1\text{-}217}$ displays a proline and charge-rich amyloid core
- Removing the amyloid core from hCPEB3 abolishes its protein synthesis regulation
- Cryo-ET of CPEB3-GFP in cells shows multi lamellar compartments and bundled filaments

Authors

Maria D. Flores, Michael R. Sawaya, David R. Boyer, ..., Jorge Cardenas, Luana Fioriti, Jose A. Rodriguez

Correspondence

mflores@mbi.ucla.edu (M.D.F.), luana.fioriti@marionegri.it (L.F.), jrodriguez@mbi.ucla.edu (J.A.R.)

In brief

Flores et al. investigate self-assembly of the hCPEB3 prion-like domain, determining the cryo-EM structure of its labile amyloid fibrils. The amyloid-forming segment is critical for the protein's translational regulation of target mRNAs and its proper distribution in cells. Overexpression of wild-type hCPEB3 is cytotoxic and induces multilamellar subcellular compartments.

Flores et al., 2025, Structure *33*, 1314–1324
August 7, 2025
https://doi.org/10.1016/j.str.2025.05.007

CellPress

CellPress
OPEN ACCESS

Structure

Article

Structural insights into functional regulation of the human CPEB3 prion by an amyloid-forming segment

Maria D. Flores,[1,*] Michael R. Sawaya,[2] David R. Boyer,[2] Samantha Zink,[1] Susanna Tovmasyan,[1] Adrian Saucedo,[1] Logan S. Richards,[1] Chih-Te Zee,[1] Jorge Cardenas,[1] Luana Fioriti,[3,4,*] and Jose A. Rodriguez[1,5,*]

[1]Department of Chemistry and Biochemistry, UCLA-DOE Institute for Genomics and Proteomics, STROBE, NSF Science and Technology Center, University of California, Los Angeles (UCLA), Los Angeles, CA 90095, USA

[2]Department of Biological Chemistry and Department of Chemistry and Biochemistry, University of California, Los Angeles (UCLA), Howard Hughes Medical Institute (HHMI), UCLA-DOE Institute for Genomics and Proteomics, Los Angeles, CA 90095, USA

[3]Department of Neuroscience, Istituto di Ricerche Farmacologiche Mario Negri, IRCCS, 20156 Milano MI, Italy

[4]Department of Neuroscience, Columbia University, New York, NY 10027, USA

[5]Lead contact

*Correspondence: mflores@mbi.ucla.edu (M.D.F.), luana.fioriti@marionegri.it (L.F.), jrodriguez@mbi.ucla.edu (J.A.R.)

https://doi.org/10.1016/j.str.2025.05.007

SUMMARY

The cytoplasmic polyadenylation-element-binding-protein-3 (CPEB3) is a functional prion thought to modulate protein synthesis and enable consolidation of long-term memory in neurons. We report a cryoelectron microscopy (cryo-EM) structure of amyloid fibrils grown *in vitro* from the first prion-like domain of human CPEB3 (hCPEB3), revealing their ordered 49-residue core, spanning L103 to F151. CPEB3 lacking that segment coalesces into abnormal puncta in cells compared to wild-type CPEB3, localizes away from dormant p-bodies and toward stress granules, and lacks the ability to influence protein synthesis in neurons. Fluorescence-guided cryo-focused ion beam (cryo-FIB) milling and cryo-electron tomography (cryo-ET) applied to neuronal cells expressing CPEB3 reveal CPEB3-GFP signal from lamellae enriched in multivesicular bodies (MVBs), cavernous multilamellar compartments, and bundled filaments, suggesting a state of induced cellular stress. Accordingly, cells expressing wild-type CPEB3 are less viable than those expressing CPEB3 without its amyloid core, suggesting human CPEB3 regulation may be required to overcome the liability associated with its self-assembly in cells.

INTRODUCTION

Prions, or proteinaceous infectious particles,[1] are stable, long-lived, pathogenic or functional assemblies present in species across the tree of life.[2] Many prions rely on an amyloid architecture to recruit naive proteins and template their conversion into ordered fibrillar β sheet-rich assemblies.[2,3] Because of their ability to adopt amyloid folds, prion-like proteins present a challenge to the proteostatic framework in neurons.[4] However, since prions can endure protein turnover, they can also influence the persistence of biochemical states that influence memory consolidation.[5]

Prion-based mechanisms have been described to influence learning and memory in *Aplysia*,[6] *Drosophila*[7,8] and most recently, mammals.[9,10] Neuronal isoforms of the cytoplasmic polyadenylation element binding protein (CPEB), a functional prion, are involved in regulating localized translation at synapses.[4] In Drosophila, prion-like fibrillar aggregates of the CPEB ortholog, Orb2 display amyloid features, including steric zipper motifs. Their dry amyloid fibril core is formed by tightly mated sheets whose glutamine side chains interdigitate. The discovery of this structure supports the theory that CPEB orthologs can form persistent or stable amyloid assemblies, but leaves unknown the origin of these assemblies, their stability in cells, and the mechanism by which they avoid cytopathology.[11] Additionally, while these studies present remarkable views of functional prion structures in invertebrates, they offer limited insights into the prion-like function of mammalian CPEBs.[6,7,10] Vertebrate CPEBs (CPEB1-4) are RNA-binding proteins that can promote the translation or repression of targets. CPEB1-4 have C-terminal RNA-binding domains and variable N-terminal domains with intrinsically disordered regions,[12] and in the case of CPEB2 and CPEB3, are Q/N-rich.

CPEB3 is known to influence memory consolidation in mice and humans.[4,9,13,14] In mice, it is a 716-residue protein with two N-terminal prion-like domains linked by a short, low-complexity regulatory motif (Figure 1A). CPEB3 contains an N-terminal low complexity domain,[8] akin to those found in functional yeast prions.[2] The CPEB3 prion domains influence the activity of its two C-terminal RNA-binding domains and zinc

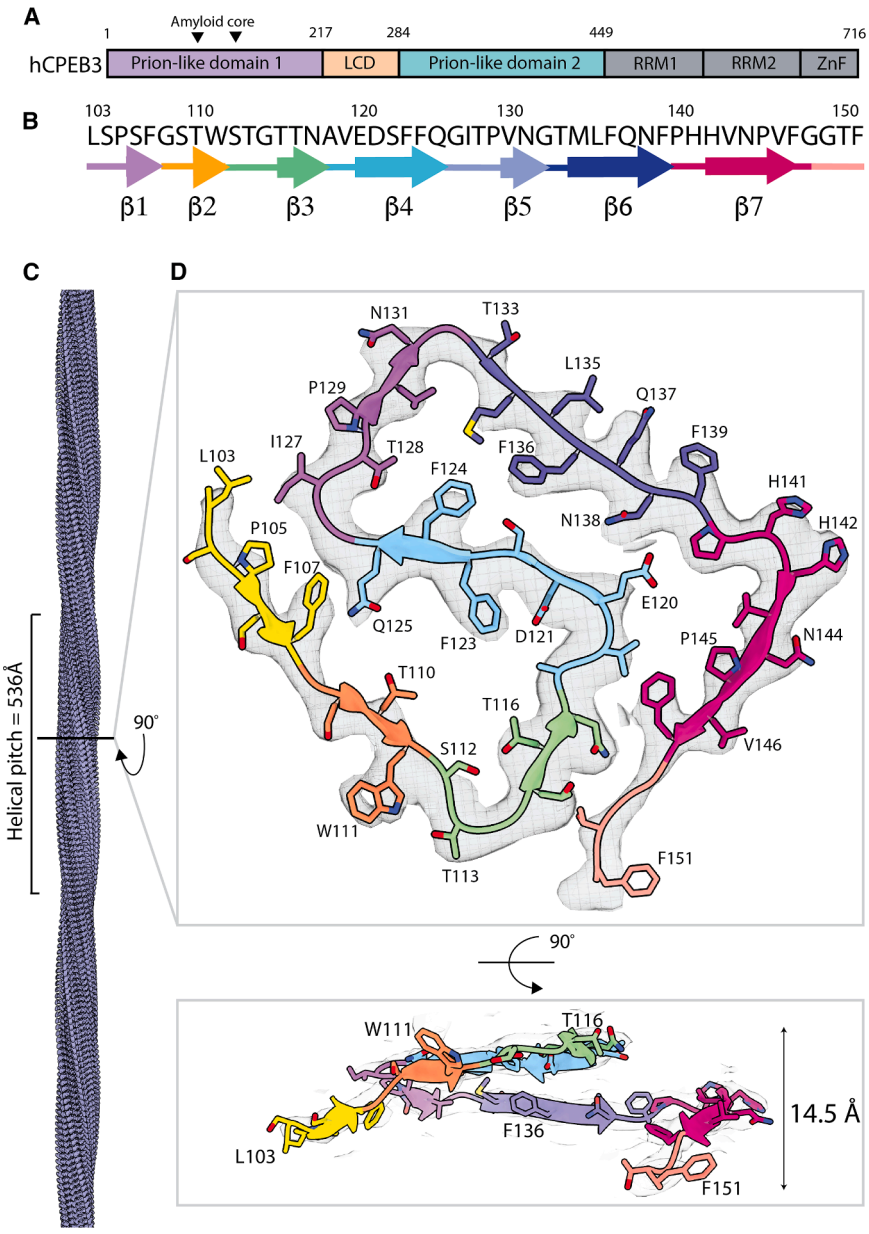

Figure 1. Cryo-EM structure of fibrils formed by the human CPEB3 prion-like domain 1

(A) Schematic summary of hCPEB3 domains.

(B) Amino acid sequence alignment of fibril core corresponding to secondary structure β strands.

(C) Model of CPEB3AC filaments with a corresponding helical pitch of 536 Å.

(D) Top: cryo-EM map of cross section perpendicular to the helical axis with model rendering colored to match secondary structure schematic. Bottom: side view of map and model measuring height different within one helical layer.

finger domain[8] (Figure 1A). As an RNA-binding protein, CPEB3 regulates translation of target mRNAs that are required for synaptic plasticity and the growth of new synaptic spines.[9,15,16] CPEB3 also regulates its own translation, and its RNA transcript forms a self-cleaving ribozyme that regulates transcriptional and translation processes.[17] CPEB3 requires its N-terminal, prion-like domain 1 (PRD1) to restore a wild-type aggregation phenotype and mediate long-term potentiation (LTP) in CPEB3-deficient cells, and to influence the persistence of memory in mice,[9] while a second prion domain (PRD2) may be involved in nuclear export and binding interactions.[16] CPEB3 aggregates are regulated in part through mono-ubiquitination[15] and SUMOylation[18]; these allow for its proper activation and repression, respectively. In its basal state, CPEB3 is SUMOylated and is postulated to undergo phase separation when it colocalizes to p-bodies where it inhibits translation of target mRNAs.[16] Upon proper signal-induced activity, it is then ubiquitinated and shuttled to polysomes where it increases translation of its targets.[16] These observations support the notion that the structure, decoration and localization of prion-like CPEB3 assemblies are linked to its function.

The prion-like nature of CPEB3 is supported by its formation of heritable aggregates in yeast.[10] Similar aggregates appear to be required for its function in neurons.[10] However, structural analyses of CPEB3 are limited. Our current view of mammalian CPEB3 prion structure is informed instead by sequence analysis and nuclear magnetic resonance (NMR) spectroscopy, where sequence analysis reveals segments in the PRD1 of human CPEB3 that may form higher-order coiled-coiled α-helical assemblies and whose self-assembly may involve actin binding.[19–21] In addition, NMR spectroscopy studies predict the presence of a β-rich ordered core formed by mouse CPEB3 spanning T101-S194, and indicate its propensity to form amyloid-like fibrils.[22] However, these studies present a limited view of the physical state of CPEB3 in cells and of the atomic structures adopted by multimeric states of the CPEB3 prion-like domain.

With the goal of improving our understanding of CPEB3 functional prion-like mechanisms, we investigated the sequence of human CPEB3 PRD1 and found it capable of self-assembling into reversible amyloid fibrils in solution. The structure of these fibrils, determined by single particle cryo-EM, showed an ordered core composed of hCPEB3 residues 103 to 151 arranged in a serpentine fold. The sequence composition of this amyloid core (AC) offered clues to its lability and possible sensitivity to environmental changes in pH. CPEB3 constructs lacking this AC sequence showed altered subcellular distribution, indicating a role for this sequence in hCPEB3 activity. This hypothesis was confirmed by the altered translational regulation of AC-deficient hCPEB3 in primary neurons. To improve our understanding of

Table 1. Cryo-EM data collection, refinement, and validation statistics

	$CPEB3_{AC}$
Data collection and processing	
Magnification	105,000
Voltage (kV)	300
Electron exposure (e–/Å^2)	52
Defocus range (μm)	1–3
Pixel size (Å)	0.86
Symmetry imposed	C1
Helical rise (Å)	4.8
Helical twist (°)	−3.32
Initial particle images (no.)	2,410,032
Final particle images (no.)	40,329
Map resolution (Å)	3.0
FSC threshold	0.143
Map resolution range (Å)	200–3.0
Refinement	
Initial model used (PDB code)	*de novo*
Model resolution (Å) FSC threshold	3
Model resolution range (Å)	200–3.0
Map sharpening *B* factor (Å^2)	−100.35
Model composition	
Non-hydrogen atoms	374
Protein residues	49
Ligands	0
Protein	
R.m.s. deviations	
Bond lengths (Å)	0.006
Bond angles (°)	0.753
Validation	
MolProbity score	1.79
Clashscore	9.26
Ramachandran plot	
Favored (%)	95.74
Allowed (%)	4.26

hCPEB3 assemblies in cells, we sought molecular snapshots of CPEB3-GFP inclusions in unstimulated U87 cells using cryo-focused ion beam (cryo-FIB) milling and correlative cryo-electron tomography (cryo-ET). We found CPEB3-GFP signal in lamellae that also contained an abundance of multivesicular bodies (MVBs) and dense fibrillar structures, vesicles, and phase-separated droplets. Collectively, our observations support a model in which hCPEB3 function is regulated in part by its AC sequence in PRD1, and offer clues into the storage and regulation of prion-like inclusions in neuronal cells.

RESULTS

CPEB3 PRD1 forms amyloid fibrils *in vitro*

Hypothesizing that CPEB3 PRD1 may form functional amyloid assemblies,[23] we expressed and isolated a construct of human CPEB3 (hCPEB3) encoding its first 217 residues that included the entirety of its conserved PRD1 (Figure S1). This region of CPEB3 in mice has been previously identified as essential for prion-seeding and heritability[10] and is essential for LTP in mice.[9] We assessed the ability of this construct ($hCPEB3_{1\text{-}217}$) to form fibrils *in vitro* by enhanced fluorescence of the amyloid-binding dye ThT and negative stain electron microscopy (Figure S2). Under denaturing conditions containing high concentrations of guanidine or urea, $hCPEB3_{1\text{-}217}$ would precipitate as a heterogeneous mix of amorphous aggregates, twisting fibrils, or flat, ribbon like sheets (Figure S3). However, in solutions containing 125 mM NaCl, 50 mM Tris-Base, 10 mM K_2HPO_4, and 5 mM glutamic acid at pH 4.5 (assembly solution), $hCPEB3_{1\text{-}217}$ produced what appeared by negative stain electron microscopy to be fibrils with a homogenous twist (Figure S2B). A survey of fibrils by atomic force microscopy (AFM) revealed a well dispersed population (Figure S3A). To pursue structure determination in the face of this lability, fibrils were vitrified within an hour of formation in assembly solution.

Structure of the hCPEB3 amyloid fibril core

Solutions containing $hCPEB3_{1\text{-}217}$ fibrils were interrogated by single particle cryo-EM, with the goal of *de novo* structure determination (Figure S5). Cryo-EM images confirmed that $hCPEB3_{1\text{-}217}$ forms rapidly twisting amyloid fibrils in assembly buffer, with a single polymorph representing over 90% of imaged particles (Figure S6A). The remaining 10% of species exhibited variable twist or no twist, and therefore eluded further classification and structure determination (Figure S6B). Two-dimensional class averages confirmed canonical amyloid features corresponding to the stacking of β sheets separated by ~4.8 Å inter-strand distances, as well as a disordered flanking region, or fuzzy coat, surrounding the fibril core (Figure S6B). Three dimensional reconstructions obtained from 40,329 boxed fibril segments yielded a 3.0 Å map that showed density for a single asymmetric protofilament that fit residues L103-F151 of CPEB3, validated through sequence threading onto map (Figures 1A and 1B; Figure S7). We refer to this structure and its corresponding core sequence as the hCPEB3 amyloid core ($hCPEB3_{AC}$).

$hCPEB3_{AC}$ fibrils adopt a helical pitch of 536 Å and a left-handed twist of −3.32° (Figure 1C and Table 1). AFM images confirmed the 268 Å helical crossover and revealed the handedness of the fibrils (Figure S3). In $hCPEB3_{AC}$ fibrils, molecules stack as strands, parallel, and in register. The tight serpentine fold adopted by the $hCPEB3_{AC}$ core is enabled by five sharp kinks interspersed between its seven β strands (Figure 1D). The core contains two hydrophobic pockets and encloses three internal solvent channels. It contains a total solvent accessible surface area per chain of 1,653 Å^2. At its N terminus, L103 contacts a surface-facing segment of a beta turn in the fibril core, making a hydrophobic pocket composed of residues P105, F107, G126, and I127 (Figure S8B). An additional hydrophobic pocket is formed by residues F124, V130, M134, and F136 (Figure S8B). The core is further stabilized by stacking of aromatic residues including W111, F139, and F151, although some appear solvent facing. Polar residues T110, S112, and T116 face the largest solvent channel buried within the fibril core. A second, smaller solvent channel is lined by a group of

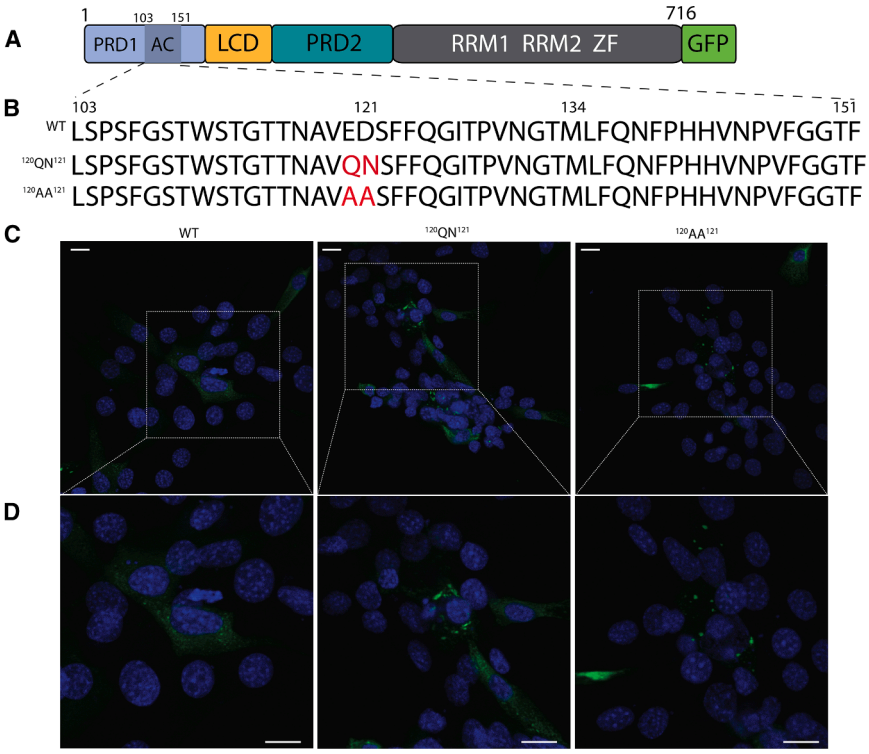

Figure 2. The role of E120 and D121 in hCPEB3 puncta formation in cells

Wild-type hCPEB3-GFP shows fine, granular like aggregates in HT22 mouse hippocampal neurons after 24 h of expression.

(A) Schematic of full-length hCPEB3 construct expressed in cells.

(B) Sequence alignment of AC region in FL constructs with corresponding mutated residues in red.

(C) hCPEB3-GFP WT and mutants (green) and nuclear staining (blue) in HT22 neurons.

(D) Insets of C. Scale bars, 10 μM.

largely hydrophobic residues: V119, P139, V143, P145; E120 stands as a lone hydrophilic residue in this group. This same glutamic acid forms part of a minute channel within the core, which is also lined by S122 and N138. The significance of E120 bridging these two solvent channels is unclear, but it could play a role in the lability of $hCPEB3_{AC}$.

Structural features of $hCPEB_{1\text{-}217}$ fibrils

Energy values calculated using coordinates of the $hCPEB3_{AC}$ show that, per layer, this core is less stable than those of pathogenic amyloids (Figure S8A).[23] Estimates of its free energy are more in line with those of fibril structures formed by reversible, functional amyloids.[24–26] Solvent facing hydrophobic residues and buried solvent channels play a role in its predicted lability, but the $hCPEB3_{AC}$ is also strained by a series of kinks. Some of these kinks tilt strands out of plane, warping the layers of the fibril to create a height difference of 14.5 Å across each of its layers (Figures 1D and S8C). While the role of warping in amyloid fibril cores remains unclear, it may help relieve the strain associated with the large twist angle observed in $hCPEB3_{1\text{-}217}$ fibrils. In addition, some kinks appear to be stabilized by local interactions. For example, a kink near G114 facilitates hydrogen-bonding between side chains of S112 and T116 (Figure 1). Four of the 28 proline residues in $hCPEB3_{1\text{-}217}$ are resolved in the core (Figure 1). The remaining 24 proline residues are unresolved in the fuzzy coat extending from the $CPEB3_{AC}$ and may function to limit the size and stability of the ordered core. They appear as smeared density in 2D averages of $hCPEB3_{1\text{-}217}$ fibrils (Figure S6B). While some of these regions are hypothesized to form coiled coils,[19] that region of the molecule remains insufficiently resolved to be assigned a secondary structure.

The role of negatively charged residues in $hCPEB_{AC}$

We observed four potentially charged residues in $hCPEB3_{AC}$: two histidine residues (H141 and H142) are solvent exposed and two acidic residues (E120 and D121) are buried within the fibril core (Figure S8A). The two histidine residues are located too far from the acidic residues for charge complementarity to stabilize the fold. E120 is located in the second solvent channel and is otherwise surrounded by hydrophobic residues, while D121 faces the opposing solvent channel (Figure S8B). As $hCPEB3_{AC}$ aggregates at a pH of 4.5, E120 and D121 are anticipated to remain protonated within the fibril core and are capable of forming stabilizing hydrogen bonds. These same residues would render the core susceptible to pH-triggered changes, as observed with other functional amyloids such as pmel17 and β-endorphin.[23,27,28] However, we found $hCPEB3_{1\text{-}217}$ fibrils to be reversible, disassembling when diluted in water (Figure S2C). ThT signal also generally diminished when $hCPEB3_{AC}$ fibrils were introduced to solutions with increased pH or as reduced ionic strength (Figure S2); a decrease in fibril abundance that was also observed by negative stain EM (Figure S4). This dissolution in response to changing environmental conditions is recapitulated by simulations tracking fibril stability over a period of 200 ns (Figure S9A). In the simulations, interlayer distances in a 5-layer fibrillar $hCPEB3_{AC}$ structure are disrupted as a pH increases from 3 to 7; notably, displacements are observed in charged residues E120 and D121 (Figure S9B).

To assess whether E120 and D121 influence the morphology, distribution, and abundance of hCPEB3 aggregates in cells, we expressed GFP-tagged full-length CPEB3 constructs encoding wild-type and E120/D121 variations, in HT22 cells (Figures 2A and 2B). In these cells, wild type, GFP-fused CPEB3 formed fine, granular fluorescent puncta, as previously described (Figures 2C, 2D, 3B, and S10A).[10,16,29] Forty-eight hours after transduction, the fine puncta were supplanted by larger puncta (Figure S10A). To probe the influence of acidic side chains at residues $^{120}ED^{121}$, we expressed a hCPEB3 variant encoding $^{120}QN^{121}$, which retains the polarity and size of the wild-type residues but ablates their negative charge. We also expressed a variant encoding $^{120}AA^{121}$ to assess the effect of ablating polarity

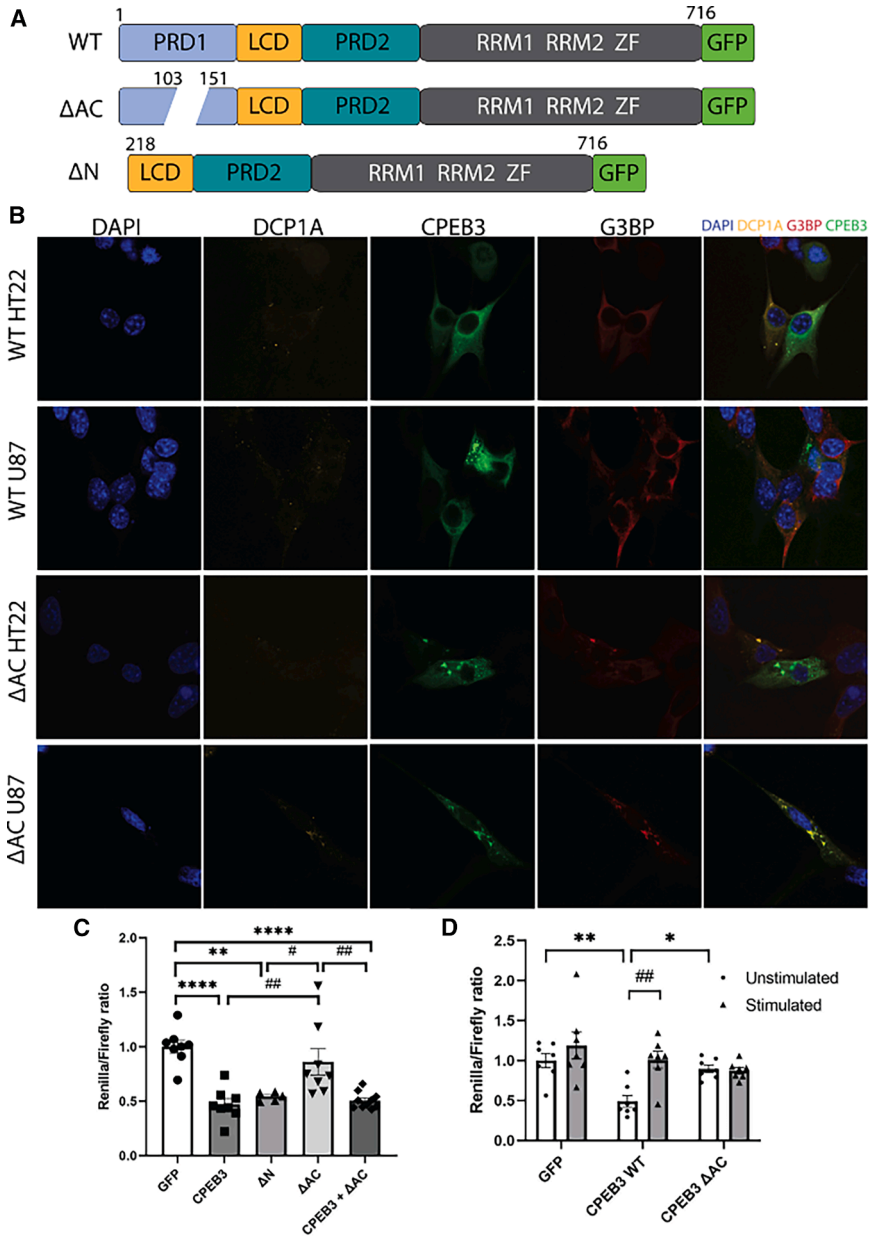

Figure 3. CPEB3$_{AC}$ regulates subcellular location of GFP-tagged hCPEB3 in cells and affects its translational regulation

(A) Schematic representation of full-length constructs used in localization and translational assays.

(B) HT22 and U87 cells expressing WT (top) and AC (bottom) (green) and subsequent co-localization with anti-Dcp1a (yellow) and anti-G3BP (red) with nuclear stain (blue).

(C) HEK 293T cells inhibitory renilla luciferase assays (n = 5–11 replicates per construct).) Graphs show the quantification of renilla/Firefly ratio, mean ± SEM. One-way ANOVA, followed by Tukey's multiple comparisons post hoc test, $^{**}p < 0.01$, $^{****}p < 0.0001$ vs. GFP; $\#p < 0.05$, $\#\#p < 0.01$, vs. CPEB3$^{\Delta AC}$.

(D) Renilla luciferase assays performed in primary neurons. (n = 7 per condition). Graphs show the quantification of renilla/Firefly ratio, mean ± SEM. Two-way ANOVA, followed by Tukey's multiple comparisons post hoc test, $^{*}p < 0.05$, $^{**}p < 0.01$, vs. CPEB3 unstimulated; $\#\#p < 0.01$ vs. CPEB3 stimulated.

and reducing the size of wild-type residues. Puncta formed by both constructs differed morphologically from those formed by wild-type CPEB3-GFP under similar conditions (Figures 2C and S10). CPEB3-^{120}QN^{121} generally formed irregularly sized and shaped puncta, while CPEB3-^{120}AA^{121} formed fewer puncta that were intermediate in size and remained more circular after 24 h (Figures 2D, S10C, S10D, and S11). The effects of these residue substitutions on the size and distribution of CPEB3$_{AC}$ puncta implicate a functional role for E120 and D121 in hCPEB3 coalescence within cells.

hCPEB3$_{AC}$ is required for proper aggregation and localization in cells

To further probe the functional relevance of hCPEB3$_{AC}$ in cells, we asked whether the presence of the AC sequence affected hCPEB3 aggregation. While CPEB3 is known to form aggregates of various sizes when overexpressed in cells,[9,10,16] a construct of hCPEB3 lacking its amyloid core, CPEB3$_{\Delta AC}$ displayed a reduced capacity to form small aggregates (Figure S10). Instead, this construct showed a delayed formation of larger aggregates as compared to wild-type hCPEB3 in HT22 cells (Figure S10). This prompted us to determine whether the localization of CPEB3$_{\Delta AC}$ differed from that of wild-type hCPEB3 in cells. Under normal conditions, CPEB3 is expected to localize in p-bodies[16] that contain mRNAs and associated regulatory proteins. There, mRNAs are stored in a dormant state while they are trafficked to their destination to be translated, or can be degraded. Alternatively, hCPEB3 could reside in stress granules (SG), induced to promote cell survival by condensing translationally stalled mRNAs.[30] We observed that wild-type CPEB3-GFP aggregates primarily colocalized with the de-capping coactivator and p-body marker, Dcp1a, in unstimulated cells (Figure 3B). In contrast, in mouse HT22 cells, aggregated CPEB3$_{\Delta AC}$ primarily colocalized with the SG assembly endoribonuclease, G3BP, and minimally colocalized with the p-body marker, Dcp1a (Figure 3B). Similar localization patterns were observed in human U87 glioblastoma cells (Figure 3B).

hCPEB3$_{AC}$ impacts translational regulation by CPEB3

CPEB3 is thought to exist in two or more distinct states that regulate its translational activity, a basal repressor state, and an aggregated or more active state.[14,31–33] In its basal state,

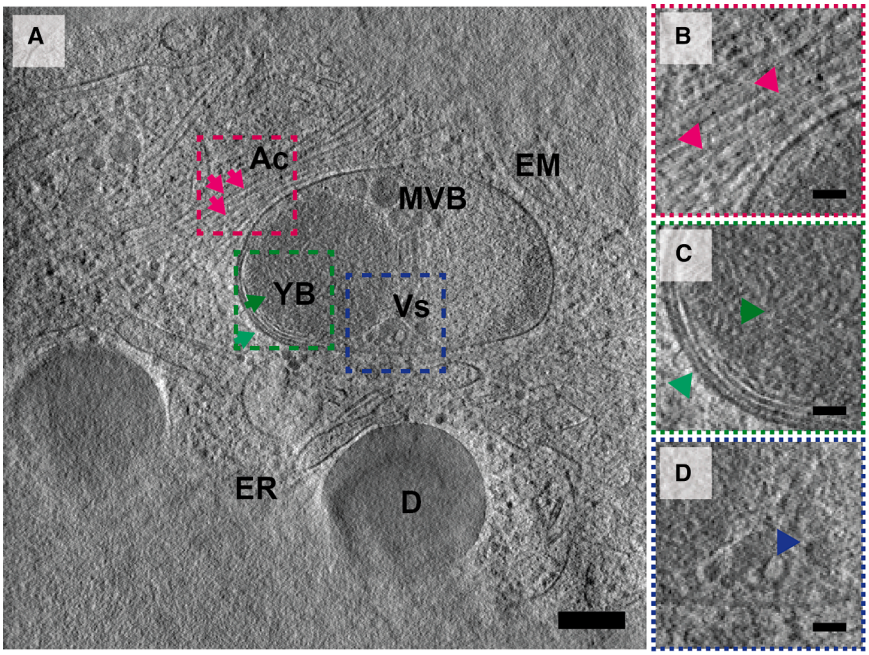

Figure 4. Cytoplasmic regions containing MVBs harbor filament-like clumps

(A) Tomographic slice from U87 cells expressing CPEB3-GFP. Where ER, endoplasmic reticulum; Ac, actin; YB, yarn ball; D, droplet; Vs, vesicle; and EM, elongated membrane. Color dashed squares highlighted in B, C, and D. Scale bar, 200 nm.

(B) Magnified inset from pink box in a, highlighting bundled actin filaments.

(C) Magnified inset from green box in a, highlighting bundled filament-like yarn balls.

(D) Magnified inset from blue box in a, highlighting small intralumenal vesicles in MVBs. Pink arrows indicate actin filaments, while dark green arrows point to yarn ball-like curly fibrils in MVBs, a light green arrow the MVB boundary, and purple arrows small vesicles. Scale bars from B, C, and D 50 nm.

CPEB3 represses translation of target mRNAs, is SUMOylated, and colocalizes to p-bodies. After neuronal stimulation, CPEB3 undergoes de-SUMOylation, leaves p-bodies, and is then shuttled to polysomes to promote translation of targets.[16] The increase in translational activity of hCPEB3 is thought to be facilitated by monoubiquitination of PRD1 by neuralized-1.[15] The ubiquitination site of CPEB3 is currently unknown and efforts to identify and characterize all SUMOylation sites[18] have not yielded a complete understanding of their role in CPEB3 activity. Since hCPEB3$_{AC}$ is situated within PRD1, we postulated it may influence translational regulation by CPEB3. In evaluation of this hypothesis, we assessed translation of CPEB3 targets, comparing the impact of wild-type protein to CPEB3$_{\Delta AC}$. Translation of Renilla luciferase fused to the 3′UTR of two established targets of CPEB3 targets, GluA2 and SUMO2 3′ UTR, in HEK-293 cells, was inhibited by both wild-type CPEB3 and CPEB3 lacking PRD1 (ΔN) (Figure 3). In contrast, translation of the same targets was unaffected by CPEB3$_{\Delta AC.}$ To evaluate whether the lack of repression was due to a loss of function, suggesting CPEB3$_{\Delta AC}$ cannot repress translation, or a gain of function, where it promotes translation without need of stimulation, we co-expressed wild type and CPEB3$_{\Delta AC}$. Co-expression of wild-type hCPEB3 and CPEB3$_{\Delta AC}$ in cells re-established the translational repression observed with the wild-type protein alone, indicating CPEB3$_{\Delta AC}$ is acting as a loss of function mutant (Figure 3C).

Expression of wild-type hCPEB3 in primary neurons repressed translation of its targets in unstimulated cells (Figure 3D). To stimulate neurons, we used a protocol consisting of bath application of bicuculline and glycine, a chemical treatment that induces long-term potentiation (LTP) of synapses (cLTP).[34] As expected, glycine-mediated cLTP induced the translation of CPEB3 targets (Figure 3D). In contrast, expression of CPEB3$_{\Delta AC}$ under the same conditions ablated all translational regulation, rendering the protein essentially inactive in this capacity (Figure 3D). In fact, luciferase activity in the presence of CPEB3$_{\Delta AC}$ was most the same as that of cells expressing GFP alone, indicating that the presence of CPEB3$_{AC}$ segment is critical in mediating a proper translation of CPEB3 targets.

Subcellular structure of U87 cells expressing CPEB3-GFP

Hypothesizing that the subcellular structure of U87 cells expressing CPEB3-GFP might offer clues into its structure and function *in situ*, we targeted fluorescent puncta in these cells for FIB milling and cryo-ET. We reconstructed tomograms from cellular lamellae with associated CPEB3-GFP fluorescence. U87 cells grown directly on EM grids and expressing CPEB3-GFP formed fluorescent inclusions; after 24 h of expression, grids were flash frozen and loaded onto a cryo-FIB-SEM instrument equipped with an integrated fluorescence objective that allowed targeting of sufficiently large cytoplasmic inclusions in cells (Figure S12). We found that GFP signal was associated with lamellae containing distinct cellular structures, including: an enrichment of multivesicular bodies (MVBs), cavernous compartments, aligned cytoskeletal filaments, autophagic bodies, and extensive networks of vesicles (Figures 4 and 5). Some of the observed MVBs contained densely packed structures, occasionally appearing to harbor fibrillar assemblies packed in tight parallel fashion and resembling yarn balls (Figures 4A and 4C). Neighboring these structures were also intralumenal vesicles and droplets (Figure 4D). Interestingly, MVBs were often found in clusters, in the vicinity of elongated membranes and droplets. Notably absent from all surveyed tomograms of CPEB3-GFP expressing cells were the large fibrillar inclusion bodies observed in cells expressing pathogenic amyloids.[35]

In addition to the yarn ball structures observed in CPEB3-GFP associated MVBs, lamellae from CPEB3 expressing cells also contained uniquely shaped, cavernous compartments (Figure 5A). These compartments were layered, but distinct from onion-like concentric lipid droplets (LDs); their layers were nearly twice the diameter of other reported striations.[36] The structures

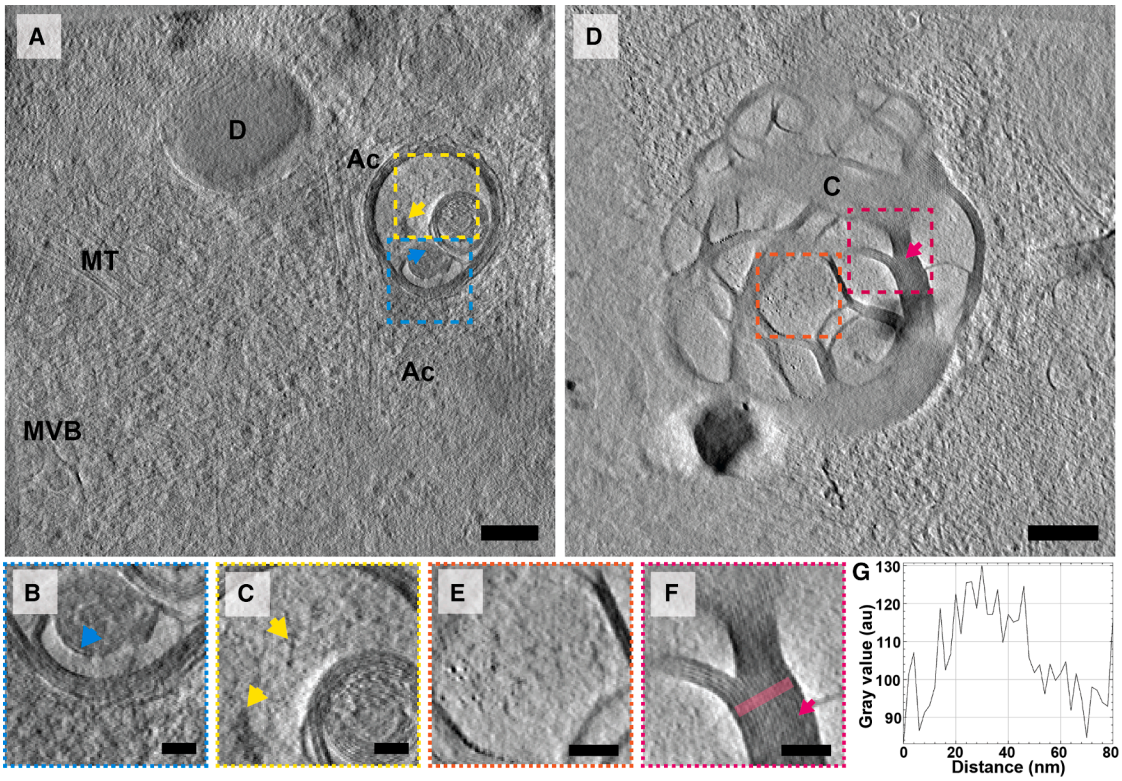

Figure 5. Ordered layers and cavities make up structured sub-compartments

(A) Tomographic slice of cytoplasmic region containing smaller compartments in U87 cells. Where MVB, multivesicular body; Mt, microtubule; D, droplet; Ac, actin; and C, compartment. Scale bar, 200 nm.

(B) Magnified inset from blue box in a, highlighting spiral entwining layers and blending of features.

(C) Magnified inset from yellow box in a, highlighting unknown densities. Scale bars, 120 nm.

(D) Tomographic slice of cytoplasmic region containing larger, cavernous compartments. Scale bar, 200 nm.

(E) Magnified inset from orange box in D, highlighting unknown densities within caverns. Scale bar, 60 nm.

(F) Magnified inset from pink box in D, highlighting ordered peripheries. Scale bar, 60 nm.

(G) Line profile of features in F, denoting regular spacing in ordered layer structure.

could also be categorized by size. A few of the compartments were less than ~0.5 μM in diameter and displayed ordered spiraled shells that entwined toward their interior (Figure 5A). The outer layers of the compartments displayed regular periodic structures. The components of these regularly spaced arrays were seen to twist toward the center of each compartment, blending into less distinguishable features (Figure 5B). Notably, the smaller compartments often contained cavernous spaces encasing poorly delineated densities (Figure 5C). We also observed ordered assemblies that formed large cavernous structures measuring up to 1 μM in diameter in surveyed lamellae (Figure 5D). Line profiles across layers of the cavernous compartment borders showed regular spacings, appearing to correspond to layered structures (Figures 5E and 5F). These characteristics were partially reminiscent of cholesteryl-ester LDs seen in mitotically arrested HeLa cells,[37] but no definitive assignment could be made for these organelles.

Persistent, exogenous expression of CPEB3 triggers cellular stress

Features observed in cells expressing exogenous CPEB3-GFP suggested a change in the physiological state of the cell. We therefore asked whether persistent exogenous expression of CPEB3-GFP could cause distress in U87 cells. We performed viability assays simultaneously staining for the apoptotic marker, annexin and 7-amino-actinomycin D, to account for necrotic cells. Using flow cytometry, we found that after 24 h of expression, approximately 13% of WT expressing cells were apoptotic, whereas cells expressing CPEB3$^{\Delta AC}$-GFP were closer to GFP control wells with 7% and 5% of cells staining positive for apoptotic marker, respectively (Figure S13A). To evaluate the molecular sequelae associated with this cellular response, we analyzed transcriptional profiles of HT22 hippocampal neurons expressing WT CPEB3-GFP, CPEB3$^{\Delta AC}$-GFP, GFP, and untreated cells. Based on normalized fold changes compared against both control samples, cells expressing CPEB3-GFP contained elevated transcripts of a variety of developmental and disease-associated genes (Figure S13B). To specifically probe the role of the CPEB3 AC, we performed a cross comparison of normalized fold changes in WT and ΔAC CPEB3-expressing cells (Figure S13B), identifying genes that were unique to WT cells. Here, we found that the majority of gene targets were involved in immune response (Figure S13B and Data S1–S4); this included differentially expressed transcripts that encoded

for guanylate-binding proteins (GBPs) functionally involved in pathogen protection responses.[38] These transcript changes and associated pathways indicate a cellular state of alert that is heightened in CPEB3-expressing cells and to a lesser extent in the absence of the hCPEB3$_{AC}$.

DISCUSSION

CPEB3, a member of the cytoplasmic polyadenylation family of proteins, binds mRNA transcripts to activate or repress protein synthesis.[39,40] This process was hypothesized to be regulated by its prion-like self-assembly,[4] although the atomic structure of prion or amyloid-like assemblies in cells by CPEB3 remained unwitnessed. We find an amyloid fibril structure of human CPEB3 PRD1 that supports the hypothesis that CPEB3 forms amyloids.[21] The ordered core of fibrils formed by this segment, hCPEB3$_{AC}$, is composed of a single asymmetric protofilament with parallel, in register strands. However, while the overall architecture of hCPEB3$_{AC}$ resembles that of a canonical amyloid structure, it contains features that may decrease its stability, including buried polar residues and solvent channels. The ready assembly of these fibrils is a potential mechanism for modulating translational regulation by CPEB3; however, we note that reparteed disassembly and re-assembly of fibrils remains unexplored.

The amino terminal domains of many CPEB proteins are identified as prion-like in part due to their low-complexity sequences and their high number of uncharged polar residues.[4,6,41] In agreement with our data, experiments have predicted that the rigid core of mouse PRD1 assemblies spans residues E124-H145, and is divided into three main β strands.[22] This is similar to the architecture of hCPEB3$_{AC}$, which contains the largest hydrophobic pockets split between four β sheets (Figures 1 and S8B). This is unsurprising, since indeed the sequences of mouse and human CPEB3 PRD1s are highly similar and are identical within the hCPEB3$_{AC}$ (Figure 1A). However, the fibrils formed by mouse CPEB3 PRD1 reportedly contained a robust and proteinase K-resistant core,[22] indicating their relatively greater sturdiness compared to hCPEB3$_{AC}$. This could be in part due to our construct containing the entire PRD1, including the proline and glutamine rich segments which are likely key contributors to the relatively labile nature of its fold. Other features that may contribute to the lability of hCPEB3$_{AC}$ include its buried charged residues (E120 and D121), its four prolines, buried solvent channels, and its highly kinked and warped layers. These features could influence the regulated assembly of amyloid-like hCPEB3$_{AC}$ structures in neurons alongside other post-translational modifications (PTMs) involved in CPEB3 regulation in cells.[15,16,18] Their relevance is supported in our double point mutant studies, where ablation of these sites altered localization of CPEB3 aggregates in cells (Figure 2).

The physiological relevance of hCPEB3$_{AC}$ is underscored by the fact that translational regulation by CPEB3 is ablated in cells when it lacks its AC. Although the structures of amyloid fibrils reconstituted *in vitro* are known to be distinct from those isolated from disease tissue,[42–46] the relevance of hCPEB3$_{AC}$ to physiological CPEB3 function remains supported by several lines of evidence. These include (1) the role of its AC sequence in localization to puncta in cells; (2) the fact that point mutations ablating charges in hCPEB3$_{AC}$ alter CPEB3 distribution in cells; (3) cellular stress and loss of viability induced by wild-type CPEB3 overproduction in cells is absent in those lacking CPEB3$_{AC}$; and most importantly, (4) that deletion of hCPEB3$_{AC}$ eliminates its ability to repress or activate mRNA targets, highlighting its role in translational activation by CPEB[9,10] (Figure 4).

Finally, by visualizing neuronal subregions harboring hCPEB3, we begin to define the ultra-structures associated its amyloid-like state. These structures include MVBs with yarn-like fibrillar inclusions and a variety of intralumenal vesicles, morphologically similar to early-stage melanosomes containing Pmel17,[28] a functional amyloid glycoprotein involved in melanin pigmentation. Lamellae in hCPEB3 expressing cells also showed distinctive compartments varying in size; all had cavernous interiors that occasionally contained unidentified densities. Many of these compartments were large enough to preclude our full mapping of their exterior, making it difficult to discern whether the caverns in these compartments were fully enclosed, or open to the cytoplasmic environment. These compartments were present in a majority of U87 cells expressing hCPEB3 and might be associated with a stress response, akin to the lipidic structures reported in stressed yeast,[36] HeLa cells[37] or potentially associated with previously reported phase separation. This is consistent with our finding that prolonged exogenous expression of hCPEB3 reduces cell viability and alters transcriptional profiles to elicit immune responses. Importantly, these deleterious effects of hCPEB3 overexpression were less evident in cells expressing CPEB3$^{\Delta AC}$-GFP, indicating that hCPEB3$_{AC}$ is a defining feature of hCPEB3 associated with cellular stress.

Overall, hCPEB3$_{AC}$ appears to be a double-edged sword that requires regulation in cells to avoid potential pathology. In fact, our collective observations of CPEB3 support a model by which the amyloid core of CPEB3 is an essential liability, a segment required for CPEB3 function but also associated with CPEB3-induced cellular stress. The localization of CPEB3 to p-bodies is sensitive to perturbations of hCPEB3$_{AC}$ and in its absence, CPEB3 localizes to stress granules. Based on these observations, hCPEB3$_{AC}$ may act as a regulatory element or may itself be subject to post-translational modifications such as SUMOylation[18] and ubiquitination.[15] Perhaps regulation of hCPEB3$_{AC}$ in turn dictates the transition of CPEB3 into and out of its prion or amyloid-like state to limit its formation of large fibrillar inclusion bodies, as observed for pathogenic protein aggregates.[35,47]

Limitations of the study

The structural data we present are drawn primarily from recombinant constructs encoding only human CPEB3$^{1-217}$, corresponding to the first CPEB3 prion-like domain.[10] This segment forms fibrils at pH 4.5, a condition that is distinct from the pH of the cell. In addition, our cellular experiments rely on exogenous expression of CPEB3-GFP, rather than endogenously tagged CPEB3 expressed at baseline levels. Further work is needed to fully understand the role of native human CPEB3 in neurons, and to further characterize structural changes occurring as it transitions from basal to its stimulated states. While we found that over time, cells expressing CPEB3-GFP grew large puncta, these same cells

suffered in viability after prolonged expression of the protein, indicating a degree of toxicity elicited by overexpression of CPEB3. Thus, our experiments highlight the need for investigation into the regulatory mechanisms that govern the CPEB3 amyloid state, and its aggregation and localization in cells.

RESOURCE AVAILABILITY

Lead contact

Further information and requests for resources and reagents should be directed to and will be fulfilled by the lead contact, Jose A. Rodriguez (jrodriguez@mbi.ucla.edu).

Materials availability

All unique/stable reagents generated in this study are available from the lead contact with a completed materials transfer agreement.

Data and code availability

- The coordinates of CPEB3-AC have been deposited in the PDB under accession code 8SPA and the map file in the EMDB with accession code EMD-40677 and are publicly available as of the date of publication. Accession codes are also listed in the key resources table. The tomograms of U87 cells expressing CPEB3-GFP are publicly available as of the date of publication under https://doi.org/10.5281/zenodo.15288496.
- This paper does not report original code.
- Any additional information required to re-process the data reported in this paper is available from the lead contact upon request.

ACKNOWLEDGMENTS

We thank Peng Ge (UCLA) for helpful discussions during cryoEM data processing, assistance during data acquisition, Duilio Cascio (UCLA) for assistance during model building and refinement, Corey Hecksel (SLAC) for assistance during data acquisition, Ambarneil Saha for assistance with RNA-seq analysis, and Po-Tao Chen for assistance in culturing primary neurons. Part of this work was performed at the Stanford-SLAC Cryo-EM Center (S2C2), which is supported by the National Institutes of Health Common Fund Transformative High-Resolution Cryo-Electron Microscopy program (U24 GM1295410). We are grateful to Wong Hoi Hui of the Electron Imaging Center for NanoMachines (EICN) for help and advice during cryoEM screening and sample preparation, and the staff of the UCLA CNSI Nano & Pico Characterization Laboratory, and thank Chensong Zhang and Jae Yang for assistance during cryo-ET data collection. Part of this work was performed at the Midwest Center for Cryo-ET (MCCET) and the Cryo- EM Research Center located in the Department of Biochemistry at the University of Wisconsin-Madison, supported by the NIH Common Fund Transformative High Resolution Cryo-Electron Microscopy program (U24 GM139168). This work was principally supported by NIH-NIGMS Grant R35 GM128867. M.D.F is supported by a Eugene V. Cota-Robles Fellowship, NIH grant GM007185, a Whitcome Pre-Doctoral Fellowship, a Audree V. Fowler Award and an NSF Graduate Research Fellowship. J.A.R. is supported as a Pew Scholar, a Beckman Young Investigator and a Packard Fellow. This work was performed as part of STROBE, an NSF Science and Technology Center through Grant DMR-1548924, and by DOE Grant DE-FC02-02ER63421.

AUTHOR CONTRIBUTIONS

M.D.F. designed experiments, purified recombinant constructs, performed negative stain EM and ThT assays, prepared cryo-EM samples, performed cryo-EM data collection and processing helical reconstruction, cultured mammalian cells, performed live fluorescence imaging, immunofluorescence experiments, performed cryo-FIB milling and cryo-ET data collection, reconstruction, and post processing. M.R.S. performed solvation energy calculations and assisted in model building and refinement. S.Z. performed computational threading and MD simulations. D.R.B. assisted in cryo-EM data processing and helical reconstruction. S.T. and A.S. analyzed and quantified fluorescent puncta. L.S.R. performed AFM experiments. T.Z. and J.C. assisted in recombinant protein expression and purification. L.F. cultured primary neurons, performed luciferase assays and analysis and guided the project. J.A.R. supervised and guided the project. M.D.F, L.F., and J.A.R. wrote the manuscript with input from all authors.

DECLARATION OF INTERESTS

J.A.R. is an equity stake holder of MedStruc Inc.

STAR★METHODS

Detailed methods are provided in the online version of this paper and include the following:

- KEY RESOURCES TABLE
- EXPERIMENTAL MODEL AND STUDY PARTICIPANT DETAILS
  - Microbe strains
  - Mammalian cell lines
- METHOD DETAILS
  - Construct design
  - Protein expression and purification
  - Fibril preparation and negative stain TEM
  - Atomic force microscopy of CPEB3 fibrils
  - Single particle cryo-EM sample preparation and data collection
  - Data processing and helical reconstruction
  - Sequence profiling
  - Energetic calculations
  - Analysis of SASA per chain
  - Molecular dynamics simulations
  - Thioflavin T-binding and dissolution assays
  - Cell culture for live imaging
  - Immunofluorescence and puncta analysis
  - Luciferase assays
  - Cryo-ET sample preparation and cryo-FIB milling
  - Cryo-ET data collection and tomographic reconstruction
  - Analysis of gene expression
- QUANTIFICATION AND STATISTICAL ANALYSIS

SUPPLEMENTAL INFORMATION

Supplemental information can be found online at https://doi.org/10.1016/j.str.2025.05.007.

Received: December 6, 2023
Revised: September 12, 2024
Accepted: May 12, 2025
Published: June 5, 2025

REFERENCES

1. Prusiner, S.B. (1982). Novel Proteinaceous Infectious Particles Cause Scrapie. Science *216*, 136–144.
2. Shorter, J., and Lindquist, S. (2005). Prions as adaptive conduits of memory and inheritance. Nat. Rev. Genet. *6*, 435–450.
3. Eisenberg, D., and Jucker, M. (2012). The amyloid state of proteins in human diseases. Cell *148*, 1188–1203.
4. Rayman, J.B., and Kandel, E.R. (2017). Functional Prions in the Brain. Cold Spring Harb. Perspect. Biol. *9*, a023671.
5. McGaugh, J.L. (2000). Memory - A century of consolidation. Science *287*, 248–251.
6. Si, K., Lindquist, S., and Kandel, E.R. (2003). A Neuronal Isoform of the Aplysia CPEB Has Prion-Like Properties. Cell *115*, 879–891.

7. Khan, M.R., Li, L., Pérez-Sánchez, C., Saraf, A., Florens, L., Slaughter, B. D., Unruh, J.R., and Si, K. (2015). Amyloidogenic Oligomerization Transforms Drosophila Orb2 from a Translation Repressor to an Activator. Cell *163*, 1468–1483.
8. Keleman, K., Krüttner, S., Alenius, M., and Dickson, B.J. (2007). Function of the Drosophila CPEB protein Orb2 in long-term courtship memory. Nat. Neurosci. *10*, 1587–1593.
9. Fioriti, L., Myers, C., Huang, Y.Y., Li, X., Stephan, J.S., Trifilieff, P., Colnaghi, L., Kosmidis, S., Drisaldi, B., Pavlopoulos, E., and Kandel, E. R. (2015). The Persistence of Hippocampal-Based Memory Requires Protein Synthesis Mediated by the Prion-like Protein CPEB3. Neuron *86*, 1433–1448.
10. Stephan, J.S., Fioriti, L., Lamba, N., Colnaghi, L., Karl, K., Derkatch, I.L., and Kandel, E.R. (2015). The CPEB3 Protein Is a Functional Prion that Interacts with the Actin Cytoskeleton. Cell Rep. *11*, 1772–1785.
11. Hervas, R., Rau, M.J., Park, Y., Zhang, W., Murzin, A.G., Fitzpatrick, J.A.J., Scheres, S.H.W., and Si, K. (2020). Cryo-EM structure of a neuronal functional amyloid implicated in memory persistence in Drosophila. Science *367*, 1230–1234.
12. Duran-Arqué, B., Cañete, M., Castellazzi, C.L., Bartomeu, A., Ferrer-Caelles, A., Reina, O., Caballé, A., Gay, M., Arauz-Garofalo, G., Belloc, E., and Mendez, R. (2022). Comparative analyses of vertebrate CPEB proteins define two subfamilies with coordinated yet distinct functions in post-transcriptional gene regulation. Genome Biol. *23*, 192.
13. Vogler, C., Spalek, K., Aerni, A., Demougin, P., Müller, A., Huynh, K.D., Papassotiropoulos, A., and de Quervain, D.J.F. (2009). CPEB3 is associated with human episodic memory. Front. Behav. Neurosci. *3*, 4.
14. Chao, H.W., Tsai, L.Y., Lu, Y.L., Lin, P.Y., Huang, W.H., Chou, H.J., Lu, W. H., Lin, H.C., Lee, P.T., and Huang, Y.S. (2013). Deletion of CPEB3 enhances hippocampus-dependent memory via increasing expressions of PSD95 and NMDA receptors. J. Neurosci. *33*, 17008–17022.
15. Pavlopoulos, E., Trifilieff, P., Chevaleyre, V., Fioriti, L., Zairis, S., Pagano, A., Malleret, G., and Kandel, E.R. (2011). Neuralized1 activates CPEB3: A function for nonproteolytic ubiquitin in synaptic plasticity and memory storage. Cell *147*, 1369–1383.
16. Ford, L., Ling, E., Kandel, E.R., and Fioriti, L. (2019). CPEB3 inhibits translation of mRNA targets by localizing them to P bodies. Proc. Natl. Acad. Sci. USA *116*, 18078–18087.
17. Chen, C.C., Han, J., Chinn, C.A., Rounds, J.S., Li, X., Nikan, M., Myszka, M., Tong, L., Passalacqua, L.F.M., Bredy, T., et al. (2024). Inhibition of Cpeb3 ribozyme elevates CPEB3 protein expression and polyadenylation of its target mRNAs and enhances object location memory. eLife *13*, e90116.
18. Drisaldi, B., Colnaghi, L., Fioriti, L., Rao, N., Myers, C., Snyder, A.M., Metzger, D.J., Tarasoff, J., Konstantinov, E., Fraser, P.E., et al. (2015). SUMOylation Is an Inhibitory Constraint that Regulates the Prion-like Aggregation and Activity of CPEB3. Cell Rep. *11*, 1694–1702.
19. Fiumara, F., Fioriti, L., Kandel, E.R., and Hendrickson, W.A. (2010). Essential role of coiled coils for aggregation and activity of Q/N-rich prions and PolyQ proteins. Cell *143*, 1121–1135.
20. Ramírez De Mingo, D., Pantoja-Uceda, D., Hervás, R., Carrión-Vázquez, M., and Laurents, D.V. (2022). Conformational dynamics in the disordered region of human CPEB3 linked to memory consolidation. BMC Biol. *20*, 9.
21. Gu, X., Schafer, N.P., Wang, Q., Song, S.S., Chen, M., Waxham, M.N., and Wolynes, P.G. (2020). Exploring the F-actin/CPEB3 interaction and its possible role in the molecular mechanism of long-term memory. Proc. Natl. Acad. Sci. USA *117*, 22128–22134.
22. Reselammal, D.S., Pinhero, F., Sharma, R., Oliyantakath Hassan, M.S., Srinivasula, S.M., and Vijayan, V. (2021). Mapping the Fibril Core of the Prion Subdomain of the Mammalian CPEB3 that is Involved in Long Term Memory Retention. J. Mol. Biol. *433*, 167084.
23. Sawaya, M.R., Hughes, M.P., Rodriguez, J.A., Riek, R., and Eisenberg, D. S. (2021). The expanding amyloid family: Structure, stability, function, and pathogenesis. Cell *184*, 4857–4873.
24. Murray, D.T., Kato, M., Lin, Y., Thurber, K.R., Hung, I., McKnight, S.L., and Tycko, R. (2017). Structure of FUS Protein Fibrils and Its Relevance to Self-Assembly and Phase Separation of Low-Complexity Domains. Cell *171*, 615–627.e16.
25. Wasmer, C., Lange, A., Van Melckebeke, H., Siemer, A.B., Riek, R., and Meier, B.H. (2008). Amyloid fibrils of the HET-s(218-289) prion form a β solenoid with a triangular hydrophobic core. Science *319*, 1523–1526.
26. Lu, J., Cao, Q., Hughes, M.P., Sawaya, M.R., Boyer, D.R., Cascio, D., and Eisenberg, D.S. (2020). CryoEM structure of the low-complexity domain of hnRNPA2 and its conversion to pathogenic amyloid. Nat. Commun. *11*, 4090.
27. McGlinchey, R.P., and Lee, J.C. (2017). Reversing the Amyloid Trend: Mechanism of Fibril Assembly and Dissolution of the Repeat Domain from a Human Functional Amyloid. Isr. J. Chem. *57*, 613–621.
28. Maji, S.K., Perrin, M.H., Sawaya, M.R., Jessberger, S., Vadodaria, K., Rissman, R.A., Singru, P.S., Nilsson, K.P.R., Simon, R., Schubert, D., et al. (2009). Functional amyloids as natural storage of peptide hormones in pituitary secretory granules. Science *325*, 328–332.
29. Ramírez de Mingo, D., López-García, P., Vaquero, M.E., Hervás, R., Laurents, D.V., and Carrión-Vázquez, M. (2023). Phase separation modulates the functional amyloid assembly of human CPEB3. Prog. Neurobiol. *231*, 102540.
30. Protter, D.S.W., and Parker, R. (2016). Principles and Properties of Stress Granules. Trends Cell Biol. *26*, 668–679.
31. Drisaldi, B., Colnaghi, L., Levine, A., Huang, Y., Snyder, A.M., Metzger, D. J., Theis, M., Kandel, D.B., Kandel, E.R., and Fioriti, L. (2020). Cytoplasmic Polyadenylation Element Binding Proteins CPEB1 and CPEB3 Regulate the Translation of FosB and Are Required for Maintaining Addiction-Like Behaviors Induced by Cocaine. Front. Cell. Neurosci. *14*, 207.
32. Hervás, R., del Carmen Fernández-Ramírez, M., Galera-Prat, A., Suzuki, M., Nagai, Y., Bruix, M., Menéndez, M., Laurents, D.V., and Carrión-Vázquez, M. (2021). Divergent CPEB prion-like domains reveal different assembly mechanisms for a generic amyloid-like fold. BMC Biol. *19*, 1–14.
33. Huang, W.H., Chao, H.W., Tsai, L.Y., Chung, M.H., and Huang, Y.S. (2014). Elevated activation of CaMKIIα in the CPEB3-knockout hippocampus impairs a specific form of NMDAR-dependent synaptic depotentiation. Front. Cell. Neurosci. *8*, 367.
34. Jaafari, N., Konopacki, F.A., Owen, T.F., Kantamneni, S., Rubin, P., Craig, T.J., Wilkinson, K.A., and Henley, J.M. (2013). SUMOylation Is Required for Glycine-Induced Increases in AMPA Receptor Surface Expression (ChemLTP) in Hippocampal Neurons. PLoS One *8*, 52345.
35. Bäuerlein, F.J.B., Saha, I., Mishra, A., Kalemanov, M., Martínez-Sánchez, A., Klein, R., Dudanova, I., Hipp, M.S., Hartl, F.U., Baumeister, W., and Fernández-Busnadiego, R. (2017). In Situ Architecture and Cellular Interactions of PolyQ Inclusions. Cell *171*, 179–187.e10.
36. Rogers, S., Gui, L., Kovalenko, A., Zoni, V., Carpentier, M., Ramji, K., Ben Mbarek, K., Bacle, A., Fuchs, P., Campomanes, P., et al. (2022). Triglyceride lipolysis triggers liquid crystalline phases in lipid droplets and alters the LD proteome. J. Cell Biol. *221*, e202205053.
37. Mahamid, J., Tegunov, D., Maiser, A., Arnold, J., Leonhardt, H., Plitzko, J. M., and Baumeister, W. (2019). Liquid-crystalline phase transitions in lipid droplets are related to cellular states and specific organelle association. Proc. Natl. Acad. Sci. USA *116*, 16866–16871.
38. Vestal, D.J., and Jeyaratnam, J.A. (2011). The Guanylate-Binding Proteins: Emerging Insights into the Biochemical Properties and Functions of This Family of Large Interferon-Induced Guanosine Triphosphatase. J. Interf. Cytokine Res. *31*, 89–97.
39. Richter, J.D. (2007). CPEB: a life in translation. Trends Biochem. Sci. *32*, 279–285.
40. Kozlov, E., Shidlovskii, Y.V., Gilmutdinov, R., Schedl, P., and Zhukova, M. (2021). The role of CPEB family proteins in the nervous system function in the norm and pathology. Cell Biosci. *11*, 64.
41. Raveendra, B.L., Siemer, A.B., Puthanveettil, S.V., Hendrickson, W.A., Kandel, E.R., and McDermott, A.E. (2013). Characterization of prion-like

conformational changes of the neuronal isoform of Aplysia CPEB. Nat. Struct. Mol. Biol. *20*, 495–501.

42. Cao, Q., Boyer, D.R., Sawaya, M.R., Ge, P., and Eisenberg, D.S. (2019). Cryo-EM structures of four polymorphic TDP-43 amyloid cores. Nat. Struct. Mol. Biol. *26*, 619–627.
43. Arseni, D., Hasegawa, M., Murzin, A.G., Kametani, F., Arai, M., Yoshida, M., and Ryskeldi-Falcon, B. (2022). Structure of pathological TDP-43 filaments from ALS with FTLD. Nature *601*, 139–143.
44. Glynn, C., Sawaya, M.R., Ge, P., Gallagher-Jones, M., Short, C.W., Bowman, R., Apostol, M., Zhou, Z.H., Eisenberg, D.S., and Rodriguez, J.A. (2020). Cryo-EM structure of a human prion fibril with a hydrophobic, protease-resistant core. Nat. Struct. Mol. Biol. *27*, 417–423.
45. Manka, S.W., Zhang, W., Wenborn, A., Betts, J., Joiner, S., Saibil, H.R., Collinge, J., and Wadsworth, J.D.F. (2022). 2.7 Å cryo-EM structure of ex vivo RML prion fibrils. Nat. Commun. *13*, 4004.
46. Kraus, A., Hoyt, F., Schwartz, C.L., Hansen, B., Artikis, E., Hughson, A.G., Raymond, G.J., Race, B., Baron, G.S., and Caughey, B. (2021). High-resolution structure and strain comparison of infectious mammalian prions. Mol. Cell *81*, 4540–4551.e6.
47. Guo, Q., Lehmer, C., Martínez-Sánchez, A., Rudack, T., Beck, F., Hartmann, H., Pérez-Berlanga, M., Frottin, F., Hipp, M.S., Hartl, F.U., et al. (2018). In Situ Structure of Neuronal C9orf72 Poly-GA Aggregates Reveals Proteasome Recruitment. Cell *172*, 696–705.e12.
48. Scheres, S.H.W. (2020). Amyloid structure determination in RELION-3.1. Acta Crystallogr. D Struct. Biol. *76*, 94–101.
49. Chaudhury, S., Lyskov, S., and Gray, J.J. (2010). PyRosetta: A script-based interface for implementing molecular modeling algorithms using Rosetta. Bioinformatics *26*, 689–691.
50. Emsley, P., Lohkamp, B., Scott, W.G., and Cowtan, K. (2010). Biological Crystallography Features and development of Coot. Acta Crystallogr. D *66*, 486–501.
51. Rohou, A., and Grigorieff, N. (2015). CTFFIND4: Fast and accurate defocus estimation from electron micrographs. J. Struct. Biol. *192*, 216–221.
52. Wagner, T., Merino, F., Stabrin, M., Moriya, T., Antoni, C., Apelbaum, A., Hagel, P., Sitsel, O., Raisch, T., Prumbaum, D., et al. (2019). SPHIRE-crYOLO is a fast and accurate fully automated particle picker for cryo-EM. Commun. Biol. *2*, 218–313.
53. Fitzpatrick, A.W.P., Falcon, B., He, S., Murzin, A.G., Murshudov, G., Garringer, H.J., Crowther, R.A., Ghetti, B., Goedert, M., and Scheres, S.H.W. (2017). Cryo-EM structures of tau filaments from Alzheimer's disease. Nature *547*, 185–190.
54. Afonine, P.V., Poon, B.K., Read, R.J., Sobolev, O.V., Terwilliger, T.C., Urzhumtsev, A., and Adams, P.D. (2018). Real-space refinement in PHENIX for cryo-EM and crystallography. Res. Pap. Acta Cryst. *74*, 531–544.
55. Alford, R.F., Leaver-Fay, A., Jeliazkov, J.R., O'Meara, M.J., DiMaio, F.P., Park, H., Shapovalov, M.V., Renfrew, P.D., Mulligan, V.K., Kappel, K., et al. (2017). The Rosetta all-atom energy function for macromolecular modeling and design HHS Public Access. J. Chem. Theory Comput. *13*, 3031–3048.
56. Eisenberg, D., and McLachlan, A.D. (1986). Solvation energy in protein folding and binding. Nature *319*, 199–203.
57. Koehl, P., and Delarue, M. (1994). Application of a self-consistent mean field theory to predict protein side-chains conformation and estimate their conformational entropy. J. Mol. Biol. *239*, 249–275.
58. Van Der Spoel, D., Lindahl, E., Hess, B., Groenhof, G., Mark, A.E., and Berendsen, H.J.C. (2005). GROMACS: Fast, flexible, and free. J. Comput. Chem. *26*, 1701–1718.
59. Vanommeslaeghe, K., Hatcher, E., Acharya, C., Kundu, S., Zhong, S., Shim, J., Darian, E., Guvench, O., Lopes, P., Vorobyov, I., and Mackerell, A.D., Jr. (2010). CHARMM General Force Field (CGenFF): A force field for drug-like molecules compatible with the CHARMM all-atom additive biological force fields. J. Comput. Chem. *31*, 671–690.
60. Cormier, M.J., and Kazuo, H. (1964). Studies on the bioluminescence of Renilla renoformis. Biochim. Biophys. Acta (BBA) - Spec. Sect. Biophys. Subj. *88*, 99–104.
61. Schaffer, M., Engel, B.D., Laugks, T., Mahamid, J., Plitzko, J.M., and Baumeister, W. (2015). Cryo-focused Ion Beam Sample Preparation for Imaging Vitreous Cells by Cryo-electron Tomography. Bio. Protoc. *5*, e1575.
62. Zheng, S.Q., Palovcak, E., Armache, J.P., Verba, K.A., Cheng, Y., and Agard, D.A. (2017). MotionCor2: anisotropic correction of beam-induced motion for improved cryo-electron microscopy. Nat. Methods *14*, 331–332.
63. Chen, M., Bell, J.M., Shi, X., Sun, S.Y., Wang, Z., and Ludtke, S.J. (2019). A complete data processing workflow for cryo-ET and subtomogram averaging. Nat. Methods *11*, 1161–1168.
64. Kremer, J.R., Mastronarde, D.N., and McIntosh, J.R. (1996). Computer visualization of three-dimensional image data using IMOD. J. Struct. Biol. *116*, 71–76.
65. Tegunov, D., and Cramer, P. (2019). Real-time cryo-electron microscopy data preprocessing with Warp. Nat. Methods *16*, 1146–1152.

STAR★METHODS

KEY RESOURCES TABLE

REAGENT or RESOURCE	SOURCE	IDENTIFIER
Antibodies		
anti-Dcp1a rabbit polyclonal	AbCam	cat#ab47811, RRID: AB_1566746
anti-G3BP mouse monoclonal	AbCam	cat#ab56574, RRID: AB_941699
Bacterial and virus strains		
Escherichia coli BL21 DE3	Thermo	EC0114
Escherichia coli DH5-alpha	Thermo	EC0112
Chemicals, peptides, and recombinant proteins		
NucBlue	Thermo	R37605
Critical commercial assays		
Halt protease inhibitor cocktail	Thermo	78438
ABClonal Stranded mRNA-seq Lib Prep kit	AbClonal	RK20301
Deposited data		
CPEB3-AC structure	This work	8SPA
CPEB3-AC map	This work	EMD-40677
Tomograms of U87 cells expressing CPEB3-GFP	This work	10.5281/zenodo.15288496
Experimental models: Cell lines		
HEK293 cells	ATCC	CRL-1573
Primary Hippocampal Neurons	This work	N/A
HT22 hippocampal neurons	Millipore Sigma	SCC129
U87 glioblastoma cells	ATCC	HTB-14
Oligonucleotides		
Primer for sequencing CPEB3 plasmids: 5′ – TAATACGACTCACTATAG – 3′	This work	N/A
Recombinant DNA		
CPEB3 1-217 in pET—24(+) vector	Twist	N/A
CPEB3-GFP	Twist	N/A
Software and algorithms		
Relion v3.1	Scheres et al.[48]	https://relion.readthedocs.io/en/release-5.0/#
Bcl2fastq v2.19.1.403	Illumina	N/A
PyRosetta Ref2015	Chaudhury et al.[49]	https://www.pyrosetta.org/
NanoScope Analysis v2.0	Bruker	http://nanoscaleworld.bruker-axs.com/nanoscaleworld/media/p/775.aspx
EPU v2.8	Thermo	N/A
ChimeraX v1.9	UCSF	https://www.cgl.ucsf.edu/chimerax/
Coot v1.21	Emsley et al.[50]	https://www2.mrc-lmb.cam.ac.uk/personal/pemsley/coot/

EXPERIMENTAL MODEL AND STUDY PARTICIPANT DETAILS

Microbe strains

E. coli strain DH5 alpha was used for mini and maxi preps, while E. coli BL21 gold for protein production. Both were cultured in luria broth unless otherwise noted.

Mammalian cell lines

HT22 hippocampal neurons and U87 glioblastomas were cultured in Dulbecco's modified Eagle's medium with 10% Fetal Bovine Serum (ThermoFisher) and 1% penicillin/streptomycin (ThermoFisher) in a tissue-culture incubator at 37°C and 5% CO2.

METHOD DETAILS

Construct design

Design of recombinant CPEB3 segment included previously reported residues critical for aggregate formation and prion-like behavior in cells.[10] CPEB3 residues 1-217 were inserted into pET—24(+) vector from TWIST biosciences. Sequences were verified via DNA sequencing (Genewiz).

Protein expression and purification

Recombinant $CPEB3_{1\text{-}217}$ was expressed in *Escherichia coli* BL21 GOLD cells. Briefly, cells were grown in LB media with 50 ug/ml kanamycin at 37°C to an OD600 of 0.6-0.8. 1 mM isopropyl B-D-1-thiogalactopyranoside (IPTG) was added for protein expression and cells were cultured an additional 6 hrs at 37°C. Cells were harvested and stored at -20°C until purification. Cell lysates were re-suspended in lysis buffer containing 10 mM Tris, 1 mM EDTA at pH 8.2 and supplemented with 1% halt protease inhibitor cocktail (Thermo Scientific), 1% homemade Benzonase and subsequently lysed using 6 consecutive freeze-thaw cycles in liquid nitrogen. Cell lysates were centrifuged (12,000gs for 30min) and pellet was resuspended in 6M guanidinium hydrochloride (Gdn-HCl), 50mM Tris-Base, 25mM imidazole at pH 8 and left gently shaking on ice overnight. Lysates were centrifuged (3,000gs for 30 min) and supernatant was filtered and loaded onto an equilibrated HisTrap HP column (GE) using NGC (Biorad). The HisTrap was pre-equilibrated with 6M Gdn-HCl, 50mM Tris-Base and 25 mM imidazole. Protein was eluted with gradient protocol containing 6M Gdn-HCl, 50mM Tris-Base and 500 mM imidazole. Eluted protein was flash frozen and stored at -80°C until further purification. Further purification was executed with RP-HPLC, using an Interchim puriFlash® 4125 Preparative Liquid Chromatography System equipped with an Interchim PT-15C8-F0040 cartridge (C8,15 μm particle size). The eluted protein fractions were defrosted from -80°C and pooled. The pooled sample was then diluted to 1.8 mL with a dilution buffer consisting of 6 M Gdn-HCl, 50 μM NaH_2PO_4, 10 μM Tris, and 20 μM imidazole. Before injection the 2-mL sample loop was washed with the above dilution buffer to maintain high concentrations of guanidine to minimize protein aggregation. [A] consisted of a 99 to 1 water to acetonitrile solution with 15 mM NH_4OH added as a buffer. [B] consisted of a 40 to 60 water to acetonitrile solution with 15 mM NH_4OH. Flow rate was set at 40 mL/min. Before injection, the system was equilibrated to 100% [A]. The protein sample was loaded onto the loop and injected. Three wavelengths were used to monitor the purification: 214 nm (black), 280 nm (orange), and 254 nm (light blue). The gradient was held at 100% [A] for 5 minutes then a gradual increase to 100% [B] was executed over a span of 25 minutes (Δ5% per minute). The target protein started eluting at 16 minutes.

Fibril preparation and negative stain TEM

Lyophilized protein powder was resuspended in water at 1.2 mg/mL concentration, aliquoted and immediately flash frozen and stored at -20°C until further use. Various buffers containing high concentrations of urea and guanidine were initially screened for fibril formation to attempt to control clumping and aggregation. Since these aggregates were heterogenous and sporadic, we instead chose to pursue conditions that yielded homogeneous aggregates by performing 96-well screens ranging in salt concentrations and pH, but without denaturants. The optimized fibril growth condition was incubation in 125mM NaCl, 50mM Tris-Base, 10mM K_2PO_4 and 5mM glutamic acid ~pH 4.5 and left shaking overnight on an acoustic resonant shaker at 37°C. Fibrils were collected by harvesting and pooling solution from wells and immediately prepared for subsequent experiments. Negative-stain transmission EM samples were prepped by applying 3 μl of fibril solution to glow-discharged 300 mesh carbon-coated formvar support films mounted on Cu grids (Ted Pella). The samples were wicked, washed briefly with water, stained with 2% uranyl acetate for 90 seconds and wicked again, allowing to air dry for 3 minutes. Grids were imaged on a T12 (FEI) electron microscope.

Atomic force microscopy of CPEB3 fibrils

CPEB3 fibrils grown overnight as described above were collected and a 15 μl aliquot of the supernatant was deposited onto freshly cleaved mica, incubated for 10 min, rinsed with 200 μl of water, and dried by nitrogen. Images were taken on a Bruker Dimension Icon microscope (UCLA CNSI Nano & Pico Characterization Laboratory) in PeakForce Tapping mode with a Scanasyst-Air-HPI probe. Images were flattened and analyzed using NanoScope Analysis 2.0 software (Bruker); their color scales were adjusted in the display image as indicated.

Single particle cryo-EM sample preparation and data collection

Freshly harvested fibril solution was diluted 5 fold with buffer containing 100mM NaCl, 10mM Tris-Base, 5mM DTT and 0.25% glycerol. 1.6 μL of diluted fibril solution was applied to each side of a glow-discharged Ultrathin carbon on Quantifoil 1.2/1.3 300 mesh on Au grid (Ted Pella) and plunge frozen into liquid ethane using a Vitrobot Mark IV (FEI) set at 100% humidity, 4°C with a blot force of -1 and blot time of 1.5 seconds. Data were collected on a Titan Krios G3i microscope with a K3 direct detection camera (Gatan) operated at an accelerating voltage of 300 keV and a 20eV slit width (BioQuantum). Automated data acquisition was performed using EPU

2.8 software (Thermo Scientific). Images were acquired with a nominal magnified pixel size of 0.86 Å/pixel, a total of 40 frames with a dose of 1.3 electrons per $Å^2$ per frame resulting in a total dose of 52 electrons per $Å^2$.

Data processing and helical reconstruction

CTF estimation were performed with CTFFIND 4.1.8.[51] Drift-correction and dose-weighting were performed using MotionCor2 implemented in RELION 3.1.[48] Particles were picked with the automatic particle picking software crYOLO.[52] All subsequent image processing and helical reconstruction were performed in RELION as previously described.[42,53] Briefly, fibril segments were initially extracted with a 90% overlap into 512 pixel boxes binned by 2 (1.72 A/pix) and subjected to reference-free 2D classification using a T=2 regularization parameter. Segments belonging to suboptimal 2D averages were discarded and homogenous subsets were selected for further processing. Upon identification of a rapidly twisting species, a smaller box size was chosen. All segments were then extracted with a 90% overlap into 384 pixel boxes for a total of 2,410,032 segments. Segments were split into 10 groups and several rounds of reference free 2D classification were performed to weed out suboptimal segments. Homogenous subsets from each were regrouped and reference free 2D classification were iteratively run decreasing psi_step and offset_step from 8 to 1. After the majority of suboptimal particles had been discarded an additional round of classification were performed with the tau regularization parameter set to T= 8. Only segments contributing to averages showing clear 4.8 Å signal in corresponding 2D FFTs were selected for subsequent 3D processing, resulting in 119,372 segments. Using both the 512 pixel box and 384 pixel box an initial helical pitch of 536 Å and helical twist of -3.22° were estimated. Starting with these estimates a 3D reference was reconstructed de-novo with 384 pixel 2D averages showing clear β-strand separation along the helical axis. 3D manual refinements were performed using a 30 Å low-pass filtered initial model, K=3 and with manual control of tau_fudge and healpix to reach a resolution of ~5Å. Segments contributing to a homogeneous class as defined by stable helicity and separation of β-strands resulted in a final subset of 40,329 segments. Again, a manual 3D refinement was performed on selected segments leading to a reconstruction of 3.5 Å. Several 3D auto-refinements using a 7Å low-pass filtered map from the final manual refinement were run with optimization of helical parameters leading to an estimated helical rise of 4.91 Å and a helical twist of -3.32°. This map was then used for per-particle CTF estimation and a 3D auto-refinement was repeated. The nominal pixel size was adjusted from 0.86 Å to 0.879 Å, resulting in an expected helical rise of 4.8 Å. Post-processing of the map with an extended initial mask of 3 pixels and soft edge of 10 pixels was followed by clipping and centering the map. Auto-sharpening using phenix.auto_sharpen at the resolution cutoff indicated by the half-map GSFSC led to a final overall resolution of 3.0 Å. The atomic model was built into the refined map using COOT.[50] We performed automated structure refinement using phenix.real_space_refine (Phenix 1.2).[54]

Sequence profiling

Sequences were threaded onto a hand-modeled backbone trace built into the fibril core density using a custom python script utilizing the PyRosetta[49] software package and a sliding window approach. For each window, the experimentally expressed sequence was threaded onto a poly-alanine backbone then energy minimized with the PyRosetta FastRelax with cryo-EM density function. FastRelax used the Ref2015[55] energy function with a modified fa_elec weight to 1.5 and elec_dens_fast weight of 25. Each sequence window was energy minimized in triplicate and the resulting scores were averaged. Symmetry was applied to pose objects to increase speed of computation.

Energetic calculations

Solvation free energy calculations were performed as recently described.[23] Briefly, the solvent accessible surface area (SASA) for each atom in a residue was determined (folded state). Next, the SASA for each atom of a residue was determined in the absence of the other residues (reference state), and the difference between both states was calculated ($SASA_{Ref}$ – $SASA_{Fold}$). This value was then multiplied by the Atomic Solvation Parameter (ASP) specific to each atom, as determined previously by Eisenberg et al.[56] An entropic term is also included to take into consideration the degrees of freedom lost in going from a disordered to ordered state.[57] The energies of all atoms were then summed to generate the solvation energy for each structure. Difference energy maps were generated by subtracting solvation free energies pairwise for each atom in the two structures being compared.

Analysis of SASA per chain

Solvent accessible surface area was calculated using a 5-layer model of the CPEB3AC fibril structure using the rolling ball method.

Molecular dynamics simulations

Molecular dynamics simulations were performed with the GROMACS[58] software package (version 2022.2) using the CHARMM27[59] all-atom forcefield. Simulations were carried out with a 5-layer CPEB fibril under varying charge states to simulate fibril dynamics at pHs 3, 5, and 7. The N- and C-termini of the fibril were capped with an acetyl and N-methyl amide group, respectively. In each case, the fibril was placed in a cubic box, solvated with SPC/E three-point water molecules and added counter ions. The system was energy minimized, then temperature and pressure equilibrated for 100 ps. Final simulations were executed for 200 ns.

Thioflavin T-binding and dissolution assays

Protein was resuspended in fibril formation buffer as described previous at 25 μM concentration with equal parts ThT. Solution was pipetted into a 96-well well plate with optical bottom (Sigma-Aldrich) and incubated at 37°C with continuous shaking. ThT

fluorescence was measure with an excitation filter of 440 nm and emission filter of 480nm using a Varioskan plate reader (ThermoFisher). Aggregation curves were generated from triplicate, n=3 wells. Dissolution assays were started after 18 hours of fibril formation. Because fibrils were not able to be resuspended in different buffers due to their liability, a 96-well plate was prepared by three-fold dilution of fibril-containing solutions into each buffer. The buffers used for dissolution experiments contained 100mM NaCl, 50mM K_2HPO_4/KH_2PO_4 with addition of NaOH for pH adjustment. Normalization of ThT intensity was performed to account for variations across experiments and reduction of signal when diluting samples for dissolution assays.

Cell culture for live imaging

Cells were plated and cultured on 12-mm glass coverslips coated with poly–L-lysine (Sigma) and Laminin 50 uG (Sigma) in 6-well cell-culture plates. Cells were plated at 70% confluency overnight and transfected using Lipofectamine 3000 kit (ThermoFisher) for an 8 hr incubation. Cells were harvested and/or imaged at 24 hours post transfection for all experiments. Live fluorescent images were acquired on an EVOS M7000 (ThermoFisher) on a 40X objective.

Immunofluorescence and puncta analysis

Cells were fixed in 2% paraformaldehyde at 4°C for 10 minutes and permeabilized using 0.5% PBS-Triton X-100 for 10 minutes. Cells were subsequently washed with PBS-T and blocked with 2% BSA, 0.5%FSG, and PBS-T solution for 1hr at room temperature. Cells were incubated with primary antibodies diluted in blocking solution for approximately 2 hours. Cells were washed with PBS-T three times before beginning incubation with secondary antibodies and washed with PBS-T. Coverslips were mounted using Prolong Glass Antifade Mountant (ThermoFisher) and allowed to dry for 72 hours. Fluorescent images were acquired on a Leica confocal SP8-STED/FLIM/FCS on a 60X water immersion objective. Puncta were manually counted and distances were manually calculated by averaging X and Y for each puncta in GFP channels. Image analyses were performed in FIJI (ImageJ).

Luciferase assays

HEK293 cells were plated at 50% confluency overnight and transfected using Lipofectamine 3000 kit (ThermoFisher) with ~0.5 μg of CPEB3 DNA, 0.5 μg of Renilla luciferase appended with GluA2 3′ UTR or SUMO2 3′UTR, and 0.5 μg of Firefly luciferase.[60]

18/24 hr after transfection, cells were lysed with 100 μl of buffer for dual luciferase assay (Promega). 20 μl of the lysates were used for the quantification of Firefly and Renilla Luciferase activity using a Luminometer (GloMax, Promega).

Hippocampal neurons cultured for 9–10 days in Neurobasal medium with B27 supplement (Invitrogen) at a cell density of 30 000–40 000/cm2 were cotransfected (Lipofectamine LTX, LifeScience) for 3 h with ~0.5 μg of CPEB3 DNA, 0.5 μg of Renilla luciferase appended with GluA2 3′ UTR, and 0.5 μg of Firefly luciferase. We used glycine to stimulate the NMDA receptors selectively, a protocol that mimics LTP induction in cultured neurons. Chem-LTP was induced as described previously.[34] Briefly, neuronal cultures were transferred from Neurobasal growth medium to extracellular solution (ECS) containing: 150 mM NaCl, 2 mM CaCl 2, 5 mM KCl, 10 mM HEPES(pH 7.4), 30 mM glucose, 0.5mM TTX, 20mM bicuculline methiodide. The transfected neurons were stimulated with 200μM glycine for 3 min and then washed for 30 minutes before lysis in 100 μl of buffer for dual luciferase assay (Promega). 20 μl of the lysates were used for the quantification of Firefly and Renilla Luciferase activity using a Luminometer (GloMax, Promega). The ratio between Renilla and Firefly is calculated for each experimental condition.

Cryo-ET sample preparation and cryo-FIB milling

Ultrathin carbon (2 nm) Quantifoil 2/1 300 mesh on Au grids or Quantifoil 2/2 300 mesh on silicon dioxide grids were glow discharged for 30 seconds and subsequently sterilized with 70% ethanol and coated with poly-L-lysine (Sigma) and Laminin 50 uG (Sigma). U87 cells were seeded and cultured as described previously in cell culture section. Neurons were transfected as previously described in cell culture section and samples were selected for vitrification by screening on an EVOS M7000 (ThermoFisher) with a 20X objective to check for CPEB3-GFP expression and distribution on grids. Selected samples were plunge frozen into liquid ethane using a Vitrobot Mark IV (FEI) set at 100% humidity, 37°C with a blot force of 10 and blot time of 15 seconds after 24 hours of expression. Grids were mounted on cryo-FIB autogrids and were loaded onto an Aquilos II cryogenic FIBSEM instrument for cryo-FIB milling (ThermoFisher).

MAPS software (ThermoFischer) was used to aid in correlation using a combination of room temperature fluorescence images and images acquired using the integrated fluorescence light microscope (iFLM) in the FIBSEM and for acquisition of a SEM medium magnification montage. Fluorescent and SEM atlases were overlaid for correlation and selection of CPEB3-GFP expressing cells. Cells were selected for milling based on puncta phenotypes and overall placement on grid squares. Grids were coated using a gas injection system with an organometallic platinum layer of ~7-10 nm and then sputter coated with platinum for ~30 seconds. Briefly, cryo-FIB milling was performed using a stepwise decreasing current (500 pA – 30 pA), manually as described previously,[61] and automatically using AutoTEM (ThermoFischer) with milling angles ranging from 8° – 15°. SEM imaging was used to monitor milling progress throughout. Final lamellae thickness ranged from 150 nm – 250 nm. Final polished lamellae were sputter coated for 15 seconds and the iFLM was used to acquire GFP fluorescence z-stacks to aid in correlation during data collection.

Cryo-ET data collection and tomographic reconstruction

Data were collected on a Titan Krios G3i microscope with a K3 direct detection camera (Gatan) operated at an accelerating voltage of 300 keV and a 20eV slit width (BioQuantum) or with a Titan Krios G4 with a Falcon4EC (ThermoFisher) and a 10eV slit width. Data were

also collected on a Talos Arctica with a K2 Summit direct detection camera (Gatan) operating at an accelerating voltage of 200 keV and 20eV slit width (BioQuantum). For lamellae with fluorescent data, medium magnification montages were acquired using SerialEM and overlaid with GFP maximum intensity projections acquired on iFLM using MAPS. Tilt series acquisition was selected for based on signal presence and intensity on lamellae. Automated data acquisition was performed using SerialEM software at a nominal magnified pixel size of 3.64 Å/pix or 4.27 Å/pix. Dose symmetric tilt series were acquired between -60° to +60° with either 2° or 3° steps. On average, 7 frames were recorded for each image for a total electron dose of ~100 - 120 $e^-/Å^2$ and a defocus target of -5 to -7 μM. Frames were aligned using MotionCor2[62] and automatically reconstructed in EMAN2.[63] Tomograms were screened and selected for based on their contents and quality and subsequently reprocessed as follows. Tilt series were aligned using fiducial-less patch tracking and reconstructed by weighted back projection in IMOD[64] binned by two, with frames containing obstructions such as ice contaminations manually removed before alignment. A CTF-based deconvolution filter was applied to each tomogram for visualization purposes.[65] Tomograms reconstructed in AreTomo are available from https://doi.org/10.5281/zenodo.15288496.

Analysis of gene expression

Samples for RNA expression were prepared as follows. HT22 cells alone as well as those expressing CPEB3 constructs were cultured as previously described, then RNA was purified using Qiagen RNeasy Mini Kit. Libraries for RNA-Seq were prepared with ABClonal Stranded mRNA-seq Lib Prep kit. Sequencing was performed on Illumina HiSeq 3000. Data quality check was performed on Illumina SAV. Demultiplexing was performed using the Illumina Bcl2fastq v2.19.1.403 software, with the Partek flow being used for data analysis. Transcript alignment was performed using STAR with reference genome mouse mm39. Ensembl Transcripts release mm39 - Ensembl Transcripts release 107 was used for gene feature annotation. Counts per Million (CPM) normalization of transcripts was followed by adding 0.0001. Partek GSA (version 3.5) was used to determine differentially expressed genes between sample set comparisons. Different P-value thresholds were used to filter for significantly differentially expressed genes. Gene Ontology enrichment was determined by ShinyGO 0.77.

QUANTIFICATION AND STATISTICAL ANALYSIS

Data are expressed as mean or median ± standard error of the mean (SEM) and graphed as scatter plots. For Violin Plots, data are expressed as median ± IQR (interquartile between 25th and 75th percentile). The GraphPad Prism 9 software was used for the statistical analysis. All data were tested for normal distribution using the Shapiro–Wilk normality test. For >2 groups, the results were analyzed by one-way or two-way ANOVA followed by Tukey's multiple comparisons test. Additional information on the tests including the number of repeats and (Avg) ± SE are stated in figure legends. The refinement statistics and other parameters associated with Cryo-EM data collection are summarized in Table 1.